



**HAL**  
open science

# Nano structure Ti-doped skutterudite CoSb<sub>3</sub> thin films through layer inter-diffusion for enhanced thermoelectric properties

Guang-Xing Liang, Zhuang-Hao Zheng, Fu Li, Jing-Ting Luo, Hao Jin, Xianghua Zhang, Ping Fan

## ► To cite this version:

Guang-Xing Liang, Zhuang-Hao Zheng, Fu Li, Jing-Ting Luo, Hao Jin, et al.. Nano structure Ti-doped skutterudite CoSb<sub>3</sub> thin films through layer inter-diffusion for enhanced thermoelectric properties. *Journal of the European Ceramic Society*, 2019, 39 (15), pp.4842-4849. 10.1016/j.jeurceramsoc.2019.06.044 . hal-02181828

**HAL Id: hal-02181828**

<https://univ-rennes.hal.science/hal-02181828>

Submitted on 18 Oct 2019

**HAL** is a multi-disciplinary open access archive for the deposit and dissemination of scientific research documents, whether they are published or not. The documents may come from teaching and research institutions in France or abroad, or from public or private research centers.

L'archive ouverte pluridisciplinaire **HAL**, est destinée au dépôt et à la diffusion de documents scientifiques de niveau recherche, publiés ou non, émanant des établissements d'enseignement et de recherche français ou étrangers, des laboratoires publics ou privés.

# Nano structure Ti-doped skutterudite CoSb<sub>3</sub> thin films through layer inter-diffusion for enhanced thermoelectric properties

Guang-xing Liang <sup>a</sup>, Zhuang-hao Zheng <sup>a,\*</sup>, Fu Li <sup>a</sup>, Jing-ting Luo <sup>a</sup>, Hao Jin <sup>a</sup>, Xiang-hua Zhang <sup>b</sup>, Ping Fan <sup>a</sup>

<sup>a</sup>. Shenzhen Key Laboratory of Advanced Thin Films and Applications, College of Physics and Optoelectronic Engineering, Shenzhen University, Shenzhen, 518060, China.

<sup>b</sup>. University Rennes, CNRS, ISCR (Institut des Sciences Chimiques de Rennes) – UMR 6226, F-35000 Rennes, France.

\* **Corresponding** Author, Email: [zhengzh@szu.edu.cn](mailto:zhengzh@szu.edu.cn)

**Abstract:** Ti-doped CoSb<sub>3</sub> thin films were prepared through layer inter-diffusion method and the prepared thin films have unique architecture, containing nano-size grains. According to the Raman analysis, the films have weaker atomic vibration after Ti doping. This nano-structure and the weak atomic vibration can scatter a wide-range spectrum of phonons, resulting the significantly decrease of thermal conductivity. In addition, this material design also leads to a very important improvement of the absolute Seebeck coefficient value, which increases from about 50  $\mu\text{VK}^{-1}$  to over 100  $\mu\text{VK}^{-1}$ . As the result, the maximum ZT value is 0.86 at 523 K for a Ti doped sample, which is six times higher than the un-doped sample and is comparable to the best value for the CoSb<sub>3</sub> based thin films. A flexible CoSb<sub>3</sub> based thin film thermoelectric generator was also fabricated and shows that the response time of all the touch events is below 1 s.

**Keywords:** Thin films, Thermoelectric, Nanostructure, layer inter-diffusion

## 1. Introduction

The confluence of energy demands and environmental preservation has stimulated research on renewable energies that will allow for an eventual energy transition away from fossil fuels as the primary source of energy [1,2]. Thermoelectric materials show great promise for applications in many fields, including direct conversion of waste heat from industrial sectors or automobile exhausts to generate electricity. They can also be used as solid state Peltier coolers [3-6]. The key characteristics for thermoelectric materials are essentially a large Seebeck coefficient  $S$ , a high electrical conductivity  $\sigma$ , and a low total thermal conductivity  $\kappa$  which is usually expressed as  $\kappa = \kappa_{lat} + \kappa_{ele}$ , where  $\kappa_{lat}$  and  $\kappa_{ele}$  are respectively lattice thermal conductivity and electrical thermal conductivity. These quantities determine the so-called dimensionless thermoelectric figure of merit,  $ZT = S^2 \sigma T / \kappa$ , where  $T$  is the absolute temperature [7]. Since the  $S$ ,  $\sigma$  and  $\kappa_{ele}$  are interrelated and conflicting via carrier concentration, it is a great challenge to largely improve the  $ZT$  value. Therefore, concepts or strategies that can decouple these parameters to simultaneously optimize the electron and phonon transport are highly encouraged and imperative for the thermoelectric community [8-10].

Skutterudite  $\text{CoSb}_3$  and its related compounds have drawn extensive attention as one of the most promising thermoelectric materials at the intermediate temperature range over the past few decades [11-15].  $\text{CoSb}_3$  crystallizes in a body-centered cubic structure with space group  $Im\bar{3}$  and a unit cell consists of 32 atoms, in which Co atoms form eight sub-cubes with pnictogen rings occupying six of them, leaving the final two voids or cages empty. It is a narrow band gap semiconductor, owning large carrier mobility, high Seebeck coefficient and complex crystal structure. However, pure  $\text{CoSb}_3$  cannot be used for thermoelectric application

because of its high thermal conductivity. Traditionally, there are two major ways to enhance its thermoelectric performance. One is to substitute Co or Sb to improve the electrical conductivity or to fill the voids in order to increase the Seebeck coefficient together with reducing the thermal conductivity by the “rattling” effect. For instance, Wang et al. demonstrated that the introduction of Yb in CoSb<sub>3</sub> can raise the ZT value from 0.5 to 1.5 at 850 K and a high average value of ~1.27 within 500 K - 850 K is obtained with the maximum Yb content of 0.29 [16]. Shi et al. reported that the multi-filling of CoSb<sub>3</sub> can lead to a maximum ZT of 1.7 at 850 K, which is several times higher than the pure sample [17]. Another way is to form low-dimensional systems, through for example nano-structuring in bulk materials, which can effectively and separately enhance the power factor ( $PF=S^2\sigma$ ) and reduce the lattice thermal conductivity  $\kappa_{lat}$  due to the more drastic phenomenon of amplified wide-range phonon scattering at the interfaces and grain boundaries. For example, Khan et al. revealed that the ZT can be doubled because of the nano-micro porosity effect and Zhou et al. shown that the ZT is 30% higher in comparison to the Ba filled CoSb<sub>3</sub> after inclusion of Ag nanoparticle [18-19]. Nevertheless, despite the fact that both of these two approaches can improve the thermoelectric properties of the CoSb<sub>3</sub> based materials, most of the filling materials are still using the rare earth elements and it is, in addition, hard to control the nano-structure during the preparation process.

Thin films with nano-scale grains have been demonstrated as another promising low-dimensional system that can enhance the material’s thermoelectric performance, comparable to the nano-structuring in bulk materials. For examples, Hicks et al. [20] prepared PbTe/Pb<sub>1-x</sub>Eu<sub>x</sub>Te multiple-quantum-well structure giving a  $ZT > 2.0$ , due to the quantum confinement effect. Walachova et al. [21] tested the ZT value of the nano-scale thickness thin film to be 2.65 by Haman-method. Similarly, several studies on the synthesis of CoSb<sub>3</sub> based thin films have also been done [22-25]. As an example, Bala et al. [22] reported the enhancement of thermoelectric performance of CoSb<sub>3</sub> films by fabricating the nano-structure through bilayer

reacting and ion beam mixing. Especially, this bilayer reaction approach employing the formation of metastable skutterudite compounds was achieved through controlling the crystallization of amorphous reaction intermediate. It was formed by low-temperature inter-diffusion of modulated elemental reactants, which was very efficient so that the empty cages of the  $\text{CoSb}_3$  might be filled up by any kind of elements including lanthanide elements and hafnium [26,27]. Thin film thermoelectric generator has considerable potential for applications in the microelectronic industry. This is not only because of its improved thermoelectric performance, but also its smaller size, fast response and compatibility for micro-semiconductor manufacturing [28-31].

In this work, promising design was reported for fabricating Ti doped  $\text{CoSb}_3$  thin films. Ti layer with nano thickness was prefabricated on insulating substrate and  $\text{CoSb}_3$  thin film was deposited onto this Ti layer. Then the sample was annealed for growing Ti-doped thin film. Such designed process can form a metastable compound by inter-diffusion at room-temperature [26,27] and grow the nano-structure thin film on the Ti layer which acts as the catalyst, being similar to the metal organic chemical vapor deposition (MOCVD) method for fabricating nano-structure [32]. The ultimate objective is to synthesize  $\text{CoSb}_3$  thin films with Ti filling and special nano-architecture that can improve the carrier mobility and also scatter more phonons with mid- to long-wavelength, leading therefore to the enhancement of power factor with low lattice thermal conductivity. Moreover, the flexible generator based on Ti doped  $\text{CoSb}_3$  nano thin film was also fabricated with Cu layer as electrodes and was tested as thermal detector.

## 2. Experimental Section

The Ti doped  $\text{CoSb}_3$  nano thin films were synthesized by growing on prefabricated layer approach via the magnetron sputtering. Ti target (99.99 %) and  $\text{CoSb}_3$  (99.95%) alloy target were used in a magnetron sputtering facility, equipped with a three-position rotatable target system. The sputtering angle was  $45^\circ$  and the target-substrate distance was 10 cm. The 3 cm

$\times 3 \text{ cm} \times 1.5 \text{ mm}$  BK7 glass substrate was used and cleaned by ultrasonic for 20 minutes in acetone, 10 min in absolute ethyl alcohol and 10 min in deionized water, respectively. The residual pressure was less than  $8.0 \times 10^{-4} \text{ Pa}$  and the working pressure was kept at 0.4 Pa with argon flow of 40 sccm as the working gas. A schematic representation of the process is shown in Figure S1. Firstly, Ti was deposited on the glass substrate with a very low deposition rate around  $0.3 \text{ \AA/s}$  and different thicknesses of about 10 nm, 15 nm, 20 nm, 25 nm and 30 nm have been obtained with the objective to study the influence of Ti doping concentration on the thermoelectric properties of the films. Then, the  $\text{CoSb}_3$  thin film was deposited onto the Ti layer. The deposition rate of  $\text{CoSb}_3$  thin film was around  $0.5 \text{ \AA/s}$  and the deposition time is 15 min, followed by a thermal annealing in a furnace at  $300 \text{ }^\circ\text{C}$  for 2 hours under a constant flow of argon. The thickness of all the thin films was about 400 nm. The crystalline phases were determined by X-ray diffraction (XRD) technique (D/max2500, Rigaku Corporation) with the  $2\theta$  angle range of  $10^\circ$ - $100^\circ$  under 0.02 degree per step, using  $\text{Cu K}_\alpha$  radiation ( $\lambda = 0.15406 \text{ nm}$ ), and the lattice parameters were refined using full-profile Rietveld refinement method. Room temperature Raman scattering measurements were performed by using a spectra system Lab Ram Xplora (Horiba Jobin Yvon). The laser excitation used in this work was the 514.5 nm line of an  $\text{Ar}^+$  ion laser. The micro-structure was characterized by scanning electron microscopy (SEM, Zeiss supra 55) and high-resolution transmission electron microscopy (HRTEM, FEI Tecnai F30). The composition content and distribution throughout the thickness of the film was investigated by Auger scanning system (AES, PHI-700, ULVAC-PHI). The incident angle of scanning Ar gun was  $30^\circ$  with the sputter rate of 4 nm/min for standard  $\text{SiO}_2$  sample. The electrical conductivity and Seebeck coefficient were measured in the interval of 323 K ~ 573 K by the simultaneous determination of Seebeck coefficient and electrical conductivity system (SBA458, Nezsch). The room-temperature thermal conductivity was obtained by transient hot-wire theory method (TC3000, Xiaxi Electronic Technology) with the reaction time of about 1 s ~ 2 s [33]. The carrier concentration and Hall

mobility were measured by Van der Pauw Hall measurement (HL5500PC, Nanometrics) at room temperature. The thermoelectric generator was tested as detector by using the Kethley 2400 which used the continuous monitoring mode with the interval time of 0.1 s.

Calculation details: Atomic structure, energetic, and electronic properties are analyzed based on the first-principles DFT calculations by using PAW potential which is implemented in the plane-wave basis Vienna ab initio Simulation Package (VASP). Perdew Burke Ernzerhof (PBE) within the generalized gradient approximations (GGA) is used to describe the electron exchange and correlation potential. For all calculations, 400 eV was chosen as the kinetic energy cutoff. For the structures optimization, a  $4 \times 4 \times 3$  grid was employed for the Brillouin-zone sampling to relax the supercell. The structure parameters are fully relaxed to minimize the total energy of the system until a precision of  $10^{-5}$  eV and the residual forces below  $0.02 \text{ eV/\AA}$ .

In order to determine whether Ti dopant is energetically favorable, the formation energy  $E_f$  of the Ti-doped  $\text{CoSb}_3$  supercell was calculated according to the following formula:

$$E_f = E_{Ti} - E_{pure} + n\mu_{Sb} - m\mu_{Ti} \quad (1)$$

where  $E_{Ti}$  and  $E_{pure}$  are the total energy of the supercell with and without Ti dopants, respectively.  $\mu_{Ti}$  and  $\mu_{Sb}$  are the chemical potentials of Ti atom and Sb atom.  $n$  and  $m$  are the number of replaced Sb atoms and Ti dopants, respectively.

### 3. Results and discussion

#### 3.1. Composition characterization

The results of composition analysis by using AES, are summarized in Table 1. The films with Ti content of 0.25 %, 0.57 %, 0.72 %, 0.83 % and 1.05 % were named as S1, S2, S3, S4, S5 and a  $\text{CoSb}_3$  thin film without Ti doping, named S0, was also fabricated for comparison. Additionally, the content of elements of sample S5 as a function of film depth was measured by AES and the result is provided in Figure S2. It can be found that the atomic ratio of Co :

Sb deviates from the stoichiometric 1:3 with a slight deficiency of Sb, and the Co, Sb and Ti content is homogeneous throughout the thickness of the thin film layer. The Energy dispersive spectrometer elemental mappings of sample S3 are measured and shown in Figure S3 which indicates that all the elements are homogeneously distributed in the thin films.

### 3.2. XRD spectra and Raman spectra

Figure 1(a) shows the XRD patterns of Ti doped  $\text{CoSb}_3$  thin films, including the pristine sample S0, as a function of Ti content. The major diffraction peaks of all the samples can be indexed to the body-centered cubic skutterudite phase with space group  $\text{Im-3}$  (JCPDS No. 76-0470). However, the pristine sample S0 has two additional small peaks, identified by an asterisk in Figure 1(a). These peaks can be indexed to the impurity phase  $\text{CoSb}_2$ , confirming that the S0 exhibits slight lack of Sb [33-34]. The estimated volume fraction of  $\text{CoSb}_2$  is lower than ~10 % for the S0 sample, indicating that the  $\text{CoSb}_3$  is still the primary phase in S0. No impurity phase can be observed from the diffraction patterns of Ti doped samples within the detection limit of the XRD spectrometer. The diffraction intensity increases with increasing Ti content, indicating that the skutterudite phase is better and better crystallized on the Ti layer. Moreover, it is worth noting that the diffraction peaks are more and more shifted towards lower angle, with increasing Ti content. The lattice parameters as a function of Ti contents have been calculated using the XRD data and the results are shown in Figure 1(b). The inset depicts the lattice parameters as a function of the nominal Ti contents  $x$  when the samples are defined as  $\text{Ti}_x\text{Co}_4\text{Sb}_{12}$ . As shown in Figure 1(b), the lattice parameter increases with increasing Ti content. The pristine S0 has a lattice parameter of ~ 9.0351 Å, while the value for S1, S2 and S3 increases slightly and saturates at ~ 9.0360 Å which is comparable to the lattice parameter of the pure  $\text{CoSb}_3$  reported by Dilley et al. and Ortiz et al. [35,36]. With further increase of Ti content, it rises significantly to ~9.0397 Å and ~9.0405 Å. In the previous work [33] as well as in this work, it was found that Sb is lacking in the un-doped film which contains impurity  $\text{CoSb}_2$  phase. Therefore, some Sb vacancies exist even in un-

doped CoSb<sub>3</sub> film, leading to smaller lattice cell than the stoichiometric CoSb<sub>3</sub>. After Ti diffusion, the Ti ions will preferentially occupy these empty sites, causing the lattice expansion. At a certain Ti doping level, the lattice parameter will correspond to that of the stoichiometric CoSb<sub>3</sub>. With further increasing Ti content, the empty site will be saturated and then the excess Ti ions might fill into the interstitial sites rather than the framework sites, leading the non linear expansion of the unit cell [37].

Raman analysis was taken in the range of 100 cm<sup>-1</sup> to 220 cm<sup>-1</sup> by using a laser excitation at 514.5 nm for all the specimens and the results are presented in Figure 2. According to the theoretical calculation, [38] there are eight Raman sensitive phonon vibration modes in CoSb<sub>3</sub>, identified as 2A<sub>g</sub> + 2E<sub>g</sub> + 4F<sub>g</sub>, with seven in the wave number range from 100 cm<sup>-1</sup> to 220 cm<sup>-1</sup>. The A<sub>g</sub> modes are Raman active in parallel polarizations, while the E<sub>g</sub> modes are Raman active with polarizability tensor components and the F<sub>g</sub> is “orthogonal” to E<sub>g</sub>. As shown in Figure 2, four of the seven modes were observed in the undoped S0 sample at the positions of 107 cm<sup>-1</sup>, 134 cm<sup>-1</sup>, 148 cm<sup>-1</sup> and 182 cm<sup>-1</sup>, corresponding respectively to the F<sub>g2</sub>, E<sub>g1</sub>, A<sub>g1</sub> and A<sub>g2</sub> with the theoretical predication. However, the modes are incomplete since three other modes, F<sub>g3</sub>, F<sub>g4</sub> and E<sub>g2</sub>, can not be observed. The E<sub>g2</sub> mode is related to the out-of-phase motion between two Sb<sub>4</sub> rings while the F<sub>g3</sub> and F<sub>g4</sub> modes are associated with the rotation of an axis parallel and out-of-plane of the rectangle about Sb ring [39]. Based on this analysis and along with the XRD and AES data, it was assumed that the disappeared F<sub>g3</sub>, F<sub>g4</sub> and E<sub>g2</sub> modes might be due to the deficiency of Sb and the subsequent point defects in the CoSb<sub>2</sub>. The Ti doped samples display significant changes in spectra, compared to the S0. Despite the fact that the F<sub>g2</sub>, E<sub>g1</sub> and A<sub>g2</sub> are still visible, there are two “new” peaks that can be observed at ~155 cm<sup>-1</sup> and ~ 188 cm<sup>-1</sup> in all the Ti doped samples. The peak located at ~155 cm<sup>-1</sup> is identified as the F<sub>g3</sub> mode rather than the shift by the A<sub>g1</sub> and the other “new” peak corresponds to the E<sub>g2</sub>, while the A<sub>g1</sub> disappears. This result is similar to that reported by Liu et al. and they attributed this phenomenon to the insertion of foreign atoms into the Sb sites

[38]. Therefore, it was deduced that Ti enters into the Sb site and breaks the symmetry, leading to the new vibration modes. Moreover, the  $F_{g4}$  is still not observed in the Ti doped samples. Because  $F_g$  is “orthogonal” to  $E_g$ , in the sense that when the crystal is oriented to maximize the  $E_g$  signal in parallel polarization, the  $F_g$  component is zero. Therefore, the disappeared  $F_{g4}$  must be of  $E_g$  symmetry both in the undoped and Ti doped samples [39]. The most notable change is that the Raman frequencies of the Ti doped samples have been increases by  $2\text{ cm}^{-1}$  to  $3\text{ cm}^{-1}$  and the vibration modes generate big changes with respect to  $S_0$ . The vibration modes are unchanged when the Ti content increases. This phenomenon indicates that the Ti will enter into the empty sites, which should originally be occupied by Sb and it will not continue the substitution of Sb when all of the Sb sites are completely occupied. With increasing Ti content, the phonon line width increases and the peaks are slightly shifted, demonstrating that the lattice parameter has been changed. This variation is due to the dynamic disorder produced by the effect of Ti atoms filling into the interstitial positions and acting as “rattling”. Whatever, the wider line width reveals that the atoms have weaker functional group energy which will weaken the atomic vibration, leading to the attenuation of phonon energy transmission. This mechanism can greatly decrease the contribution of phonons to the thermal conductivity.

### 3.3. First-principles DFT calculations

To further understand the status of Ti, the formation energy was analyzed based on the first-principles DFT calculations [40-42] and Figure S4 shows the side view of the structure when (left) one Sb atom is replaced by Ti, and (right) Ti atom sites at the interstitial position. The calculate results are shown in Table 2. As can be seen from the Table 2, it is much easier to substitute one Sb with a single Ti atom due to the calculated formation energy of only 0.18 eV, in good agreement with the above micro-structure analysis. It is worth noting that the formation energy decreases dramatically from 2.52 eV to 0.88 eV when one substitutional Ti atom is nearby. Moreover, it further decreases to 0.08 eV when two substitutional Ti atoms

are nearby, which is lower than the formation energy value of the substitute one Sb with a single Ti atom. Thus, it can be concluded that Ti atoms are likely to form clusters with the increase of Ti atoms. The Sb sites will be substituted firstly at the low concentration of Ti. Along with further increase of Ti concentration, the newly injected Ti atoms will form clusters with the original Ti atoms and occupy interstitial sites.

### 3.4. SEM and HRTEM micrographs

Figure 3 displays the SEM images for the samples S0, S1 and S3. The surface morphology of S0 seems smooth and flat, but there is no obvious crystalline grain and some porous defects can be observed. However, significant changes in the surface morphology have appeared for the Ti doped samples. For the S1, globular like nano grains extend throughout the surface. The grains are uniform and the average grain size is about 20 nm. Meanwhile, some irregular gaps between the grains with a few tens of nanometers wide and hundred nanometers long are produced. Similar result has been obtained for sample S3. In comparison with the pristine S0, such a difference is anticipated based on the fact that the thin film grown on the crystalline Ti nano layer is favored for grain growth compared to the thin film grown on amorphous substrate. The nano grain size and density increase significantly with the increase of the Ti layer thickness. It confirms that this growing mode can efficiently control the size of the nanostructure by adjusting the thickness of the prefabrication Ti layer.

Figure 4(a) shows the high resolution HRTEM image of the sample S3, confirming the well crystallized structure of the nano-grains. The HRTEM image implies that the thin film displays an inter-planar distance of 0.289 nm corresponding to the (013) plane of skutterudite  $\text{CoSb}_3$ . The selected-area Fast Fourier Transform (FFT) pattern (inset) from the red marked area further confirms the  $\text{CoSb}_3$  crystalline phase. In addition, a few nano white regions embed in the matrix can be observed (white marked area). They exhibit sphere-like nano grains and the size is around 5 nm ~ 20 nm which is in good agreement with the SEM result. Hence, the SEM micrographs and the HRTEM result prove that the concept of growing films

on a precursor crystalline nano-layer is a promising method for preparing high density nano structured thin films.

In fact, the surface characteristic is among the most important parameters for films having only hundreds-nanometer thickness [43]. Such dense nano particles in the films will provide more scattering centers to the propagation of phonons. For a better illustration, the AFM and SEM image of the precursor Ti layer with the thickness of 20 nm had been appended as Figure 4(b). The SEM result shows that tiny grains are dispersed on the thin film surface and they form a kind of independent islands in the AFM image. Based on a reported thin film growth model, [44,45] the mechanism used here for growing thin film with nano-architecture is also proposed in Figure 4(c). Generally, the thin film is Volmer-Weber growth (known as island growth) at insulate and amorphous substrate. The islands will be connected to each other to form a layer at a critical layer thickness which is highly dependent on the deposition method and parameter. The critical thickness is generally around ten nanometers in many cases. Therefore, the Ti precursor layer as shown in Figure 4(b) have many tiny grain islands when the thickness approaches to the critical layer thickness, as shown in the first stage (1) in Figure 4(c). When the  $\text{CoSb}_3$  is deposited onto this Ti precursor layer, it will grow with the Stranski-Krastanovs (SK) growth (layer and island growth) mode as shown in the stage (2). Due to the low diffusion energy at room temperature and without thermal annealing, it is likely that Ti atoms start to fill the vacancy rather than substitute other atoms. In addition, the inter-diffusion just arises around the interface, indicating that the metastable compounds are already formed at the interface [26, 27]. During the annealing process of the stage (3), the inter-diffusion is intensified across the interface, together with the grain growth. At an early stage, the metastable compounds around the interface are in equilibrium and are incompletely crystallized. Then the grains will grow with a kind of epitaxial growth process. At this stage, the grain will grow preferentially on the nano particles existing on the surface of the precursor Ti layer. The crystal growth is probably limited by diffusion because of the existence of a

high number of Ti nano-spheres acting as nucleating agent. This growth mode will lead to islands-type surface morphology with progressively decreasing gaps as the islands grow. This type of structure will slow down the phonon propagation, with the final objective to decrease significantly the thermal conductivity.

### 3.5. Electronic properties

Figure 5(a) displays the room temperature carrier concentration  $n$  and Hall mobility  $\mu$  for all the samples and Figure 5(b) shows the temperature dependence of electrical conductivity  $\sigma$ . The Hall measurement results indicate that the S0 is N-type semi-conductor and it changes to P-type conduction after Ti doping. This can be explained by the fact that Ti with four electrons in the outer shell is less than the Sb. Consequently, it will leave holes when it occupies the Sb position. Therefore, it acts like an acceptor and causes the change of the conduction type [46]. For the same reason, the  $n$  decreases as seen in Figure 5(a). However, the excess Ti atoms will provide more holes which will lead the increasing  $n$  again when it acts as the “filler”. This is why the  $n$  of S4 and S5 raises. Undoubtedly, the mobility  $\mu$  has the opposite change with respect to the  $n$ . All the mobility values of Ti doped samples are higher than the un-doped sample. It is easily understandable that the  $\mu$  and  $n$  are conflicting with similar structure. In some reports, the authors mentioned that the carrier mean-free path (2~5nm) is much shorter than the mean-free path of phonons and the size of the samples (around 10~20 nm), leading to the  $\mu$  maximum [47-49]. As shows in Figure 5(b), the  $\sigma$  decreases after Ti doping due to the decreased  $n$ . In the temperature range from 300 K to 583 K, all specimens show an increasing trend with the increasing temperature, indicating the characteristic semiconductor conduction behaviour. The un-doped sample S0 has a maximum  $\sigma$  of  $\sim 4.01 \times 10^4 \text{ Sm}^{-1}$  and the vale for samples S1 to S5 is respectively  $\sim 2.50 \times 10^4$ ,  $\sim 2.21 \times 10^4$ ,  $1.97 \times 10^4$ ,  $1.75 \times 10^4$  and  $\sim 2.10 \times 10^4 \text{ Sm}^{-1}$  at 583 K.

### 3.6. Thermoelectric performance

Figure 6(a) displays the temperature dependence of the Seebeck coefficient  $S$ . A negative  $S$  of  $S_0$  and the positive value of all the Ti doped samples can be observed due to the change of minority charge carrier as discussed above with the Hall effect analysis. As the content of Ti increases, the  $S$  increases gradually, ranging from about  $50 \mu\text{VK}^{-1}$  of  $S_1$  to over  $100 \mu\text{VK}^{-1}$  for  $S_2$ ,  $S_3$  and  $S_4$ , but reduces to  $75 \mu\text{VK}^{-1}$  at room temperature when the content of Ti is over 1.0 %. Unexpectedly, the variation trend of the  $S$  is identical with the mobility  $\mu$  and the enhancement of mobility should be benefit to  $S$ , according to Mott, that can be expressed as [50]

$$S = \frac{T\pi^2\kappa_B^2}{3q} \left( \frac{d\ln N(E)}{dE} + \frac{d\ln \tau(E)v(E)^2}{dE} \right)_{E=E_F} \quad (2)$$

Here  $N(E)$  and  $\tau$  are the electronic density of states and relaxation time, respectively. One benefits from the first term in the above equation due to the band bending at the interface with nano-inclusion, which does produce a scattering potential that might preferentially scatter low energy charge carriers, just as was the case with Pb nanoparticles in PbTe [51]. Additionally, all the Ti-doped samples have the same trend that is, the  $S$  increases with increasing temperature, with a maximum  $S_{\text{max}}$ , around 500 K – 550 K. This maximum  $S_{\text{max}}$  can be estimated by the energy gap  $E_g$  of the electronic density of states at the proximity of the Fermi energy, using [52]

$$S_{\text{max}} \propto \frac{E_g}{2eT_{\text{max}}} \quad (3)$$

where  $e$  is the elementary charge and  $T_{\text{max}}$  is the absolute temperature for  $S_{\text{max}}$ . Actually, the band gap obtained from the extrapolating the linear part of the spectrum [53]. The optical band gap can be determined from the measured fundamental absorption of the thin film by extrapolating the linear part of the spectrum  $(\alpha h\nu)^2 = f(h\nu)$  to zero and the results are shown in Figure S5. The optical band gap of the Ti-doped films is about 0.84 eV, 0.89 eV and 0.87 eV for  $S_1$ ,  $S_3$  and  $S_5$ , respectively. Thus the similar change is well in agreement with the shift of the  $S_{\text{max}}$ , suggesting that the change of the  $S_{\text{max}}$  is attribute to the change of band gap.

Figure 6(b) is the room temperature total thermal conductivity  $\kappa$  and the calculated lattice thermal conductivity  $\kappa_{lat}$ . The  $\kappa = \kappa_{lat} + \kappa_{ele}$ , where the  $\kappa_{ele}$  is the contribution of electrons and  $\kappa_{lat}$  is due to the heat transported by phonons. The  $\kappa_{ele}$  is estimated using the Wiedemann–Franz (WF) law  $\kappa_{ele} = L\sigma T$ , where the constant L, known as the Lorenz number, depends on the degree of elasticity in carrier scattering. The temperature dependence of Lorenz number was calculated and the results are provided in Table S1 [54-55]. The total  $\kappa$  of the samples S1 to S5 is respectively 0.93, 0.75, 0.62, 0.60 and 0.79  $\text{Wm}^{-1}\text{K}^{-1}$  which is about 25 %, 40 %, 50 %, 53 % and 37 % lower than the un-doped S0. Based on the WF law, the  $\kappa_{ele}$  is around 15 % of the total  $\kappa$ , indicating that the reduction of  $\kappa$  is mainly due to the sharply decrease of the  $\kappa_{lat}$ . As expected, the  $\kappa_{lat}$  follows approximately the same trend as the  $\kappa$  as a function of Ti content. All of the Ti doped samples have much lower  $\kappa_{lat}$  than the pristine sample and the S4 has the minimum  $\kappa_{lat}$ . These results indicate that the nano-structuration in  $\text{CoSb}_3$  through Ti doping can achieve a dramatic reduction of  $\kappa_{lat}$ . This has been predicted by the weakened phonon interaction from Raman spectra and by the larger phonon scattering from the SEM and TEM analysis discussed earlier. The mechanism for the reduction of thermal conductivity is schematically illustrated in Figure 6(c). Longer wavelength phonons are effectively scattered by the nano grains and gaps with larger size. Besides, the shorter wavelength phonons can be scattered by the point defects by the “rattling” effect or the lattice distortion due to the Ti doping. Similar analysis can be found elsewhere. For example, Sun et al. [37] reported that the thermal conduction in skutterudites is mainly achieved by waves associated with the vibrations of Sb. The distortion of the Sb ring structure by Te replacing some Sb is clearly not only the major perturbation of the lattice phonon spectrum but also an efficient source of point defect scattering. Figure 6(d) shows the temperature dependence of the ZT value. The pristine sample S0 has an extremely low ZT value of 0.005 at room temperature and it gradually increases to over 0.02 for all the Ti doped thin films, and S2 has the

maximum ZT value of 0.10 at room temperature. To obtain the temperature dependence of the ZT value, the  $\kappa_{ele}$  was calculated from the measured values of  $\sigma$  with fixed  $\kappa_{lat}$  value. The estimated maximum ZT of about 0.86 is achieved for the S3 sample at 523 K and this value is comparable to the best value for thin films prepared by other methods. In fact, this ZT value is likely underestimated mainly due to the overestimated  $\kappa_{lat}$ . In general, the  $\kappa_{lat}$  should have at least 50 % reduction at the testing temperature range, meaning that the real ZT value could be  $\sim 1.5$ . However, the ZT value of CoSb<sub>3</sub> thin films can demonstrate almost six times enhancement by controlling its nanostructure and morphology through appropriate Ti doping.

### 3.7. Flexible thermoelectric generator

The developed Ti doped CoSb<sub>3</sub> thin films exhibit relatively high Seebeck coefficient and it should have high thermal sensitivity due to the high carrier mobility, which is favorable for thermal detector applications. Therefore, a flexible thermal detector has been fabricated and tested as a proof of concept. To fabricate the flexible thermal electric generator, the glass substrate was replaced by kapton type polyimide substrate and the preparation parameters of the S2 sample have been chosen due to its highest performance. Two Cu layer contacts are deposited with the width of 0.25 cm in coplanar configuration and a separation of 2.5 cm. Figure 7 demonstrates the continuous response of the detector with the peaks corresponding to the values obtained when the finger touched instantly the region of the Cu contact. The finger touch event duration is about 1~2 s with 10 s interval between two events. It shows that a rise time of all the touch events is below 1 s, indicating that the detector has a fast response. It will take about 2 s to reach the maximum value, including the 0.5 s delay between the touch and departure moment. The rising time of 2 s is at least partially due to the heat transfer delay to the sensor. The sensor has stable maximum output voltage of about 0.3 mV, indicating that the thermal gradient is about 2 K at the ambient temperature of about 300 K. This sensor can be used for fast/real-time human touch electrical trigger/detector using standard electronics to read the output voltage.

#### 4. Conclusion

In summary, Ti doped  $\text{CoSb}_3$  were synthesized by depositing  $\text{CoSb}_3$  films onto Ti layer with different thicknesses. It was found that dense nano-particles are dispersed on the thin film surface and the Ti fills into the voids. As expected, these particular nanostructure and surface morphology play an important role in the increase of the Seebeck coefficient and in the significant reduction of thermal conductivity. These improvements result in an enhanced ZT, which is about six times higher than the un-doped sample. It also demonstrates the efficiency of this innovative technique for preparing high performance thermoelectric thin film. Indeed, it gives the possibility to simultaneously improve the Seebeck coefficient and to reduce the thermal conductivity through careful controlling of the structure and the morphology during the thin film deposition. It is also demonstrated that the doped material can be used as efficient and fast thermal sensor.

#### Acknowledgements

This work is supported by National Natural Science Foundation of China (No. 11604212), Key platform and research projects, Education and Research of Guangdong Province (2015KQNCX139), and Shenzhen Key Lab Fund (ZDSYS 20170228105421966). The authors thank Pro. D.Y. Gui and Dr. Y.Y. Zhong for the testing and verification of thin film thermal conductivity.

#### References

- [1]. M. S. Dresselhaus, I. L. Thomas, *Nature* 2001, 414, 332.
- [2]. S. Chu, A. Majumdar, *Nature* 2012, 488, 294.
- [3]. D.M. Rowe, *CRC handbook of thermoelectrics*, CRC press, USA 1995.
- [4]. D.M. Rowe, *Thermoelectrics handbook*, CRC press, USA 2006.
- [5]. H.J. Goldsmid, *Introduction to thermoelectrics*, Spring, England 2010.
- [6]. G. Chhatrasal, K.K. Kamal, *Prog. Mater. Sci.* 2016, 83, 330.

- [7]. G. Chen, M. S. Dresselhaus, G. Dresselhaus, J.P. Fleurial, T. Caillat, *Int. Mater. Rev.* 2013, 48, 45.
- [8]. A.J. Minnich, M.S. Dresselhaus, Z.F. Ren, G. Chen, *Energ. Environ. Sci.* 2009, 2, 466.
- [9]. S.B Riffat. X.l. Ma, *Appl, Therm. Eng.* 2003, 23, 913.
- [10]. M. Christensen, A.B. Abrahamsen, N.B. Christensen, F. Juranyi, N.H. Andersen, K. Lefmann, J. Andreasson, C.R.H. Bahl, B.B. Iversen, *Nat. Mater.* 2008, 7, 811.
- [11]. J.O. Sofo, G. D. Mahan, *Phys. Rev. B* 1998, 58, 15620.
- [12]. J. L. Feldman, D. J. Singh, *Phys. Rev. B* 1996, 53, 6273.
- [13]. X. Shi, J. Yang, J.R. Salvador, M.fang Chi, J.Y. Cho, H.Wan, S. Bai, J. Yang, W. Zhang, L. Chen, *J. Am. Chem. Soc.* 2011, 133, 7837.
- [14]. G.J. Snyder, E.S. Toberer, *Nat. Mater.* 2008, 7, 105.
- [15]. T. Caillat, A. Borshchevsky, J.P. Fleurial, *J. Appl. Phys.* 1996, 80, 4442.
- [16]. S. Wang, J.R. Salvador, J. Yang, P. Wei, B. Duan, J.H. Yang, *NPG Asia Mater.* 2016, 8, 285.
- [17]. X. Shi, J. Yang, J.R. Salvador, M.fang Chi, J.Y. Cho, H.Wan, S. Bai, J. Yang, W. Zhang, L. Chen, *J. Am. Chem. Soc.* 2011, 133, 7837.
- [18]. A.U. Khan, K. Kobayashi, D.M. Tang, Y. Yamauchi, K. Hasegawa, M. Mitome, Y. Xue, B. Jiang, K. Tsuchiya, D. Golberg, Y. Bando, T. Mori, *Nano Energy* 2017, 31, 152.
- [19]. X.Y. Zhou, G.Y. Wang, L. Zhang, H. Chi, X.L. Su, J. Sakamoto, C. Uher, *J. Mater. Chem.* 2012, 22, 2958.
- [20]. L. Hicks, T. Harman, X. Sun, M. Dresselhaus, *Phys. Rev. B* 1996, 53, 10493.
- [21]. J. Walachová, R. Zeipl, J. Zelinka, V. Malina, *Appl. Phys. Lett.* 2005, 87, 081902.
- [22]. M. Bala, C. Pannu, S. Gupta, T.S. Tripathi, S.K. Tripathi, K. Asokan, D.K. Avasthi, *Phys. Chem. Chem. Phys.* 2015, 17, 24427.
- [23]. Z.H. Zheng, P. Fan, G.X. Liang, D.P. Zhang, *J. Alloys Compd.* 2015, 619, 676.
- [24]. J. C. Caylor, A. M. Stacy, R. Gronsky, T. Sands, *J. Appl. Phys.* 2001, 89, 3508.

- [25]. S.R.S Kumar, D. Cha, H.N. Alshareef, J. Appl. Phys. 2011, 110, 083710.
- [26]. M.D. Hornbostel, E.J. Hyer, J. Thiel, D.C. Johnson, J. Am. Chem. Soc. 1997, 119, 2665.
- [27]. B. Mercey, P.A. Salvador, W.Prellier, T.D. Doan, J. Wolfman, M. Hervieu, B. Raveau, J. Mater. Chem. 1999, 9, 233.
- [28]. M. Tan, Y. Deng, Y. Hao, Energy 2014, 70,143.
- [29]. R. Venkatasubramanian, E. Siivola, T. Colpitts, B. O'Quinn, Nature 2001, 413, 597.
- [30]. P. Fan, Z.H. Zheng, Z.K. Cai, T.B. Chen, P.J. Liu, X.M. Cai, D.P. Zhang, G.X. Liang, J.T. Luo, Appl. Phys. Lett. 2013, 102, 033904.
- [31]. Z. Lu , M. Layani , X. Zhao , L.P. Tan , T. Sun , S. Fan , Q. Yan , S. Magdassi, H.H. Hng, Small 2014, 17, 3551.
- [32]. W.R. Moser, Advanced Catalysts and Nanostructured Materials: Modern Synthetic Methods, Academic press, USA 1996
- [33]. Z.H. Zheng, P. Fan, Y. Zhang, J.T. Luo, Y. Huang, G.X. Liang, J. Alloys Compd. 2015, 639, 74.
- [34]. P. Fan, Y. Zhang, Z.H. Zheng, W.F. Fan, J.T. Luo, G.X. Liang, D.P. Zhang, J. Electro. Mater. 2015, 44, 630.
- [35]. N. Dilley, E. Bauer, M. Maple, B. Sales, J. Appl. Phys. 2000, 88, 1948.
- [36]. B.R. Ortiz, C.M. Crawford, R.W. McKinney, P.A. Parilla, E.S. Toberer, J. Mater. Chem. A 2016, 4, 8444.
- [37]. H. Sun, X. Jia, L. Deng, P. Lv, X. Guo, Y. Zhang, B. Sun, B. Liu, H. Ma, J. Mater. Chem. A 2015, 3, 4637.
- [38]. H.D. Lutz, G. Kliche, Z. Anorg. Allg. Chem. 1981, 480, 105.
- [39]. G. S. Nolas. C.A. Kendziora, H. Takizawa, J. Appl. Phys. 2003, 94, 7440.
- [40]. P.E. Blöchl, Phys. Rev. B 1994, 50, 17953.
- [41]. J.P. Perdew, K. Burke, M. Ernzerhof, Phys. Rev. Lett. 1996, 77, 3865.
- [42]. J.P. Perdew and Y. Wang, Phys. Rev. B 1992, 45, 13244.

- [43]. M. Shtein, J. Mapel, J.B. Benziger, S.R. Forrest, *Appl. Phys. Lett.* 2002, 81, 268.
- [44]. J.L. Vossen, W. Kern, *Thin film processes II*, Academic press, USA 1991
- [45]. C. Argile, G.E. Rhead, *Surf, Sci, Rep.* 1989, 10, 277.
- [46]. L. Tao, X. Su, Y. Yan, G. Zheng, Q. Zhang, H. Chi, X. Tang, U. Ctirad, *J. Mater. Chem. A* 2014, 2, 17914.
- [47]. A.J. Minnich, M.S. Dresselhaus, Z.F. Ren, G. Chen, *Energ. Environ. Sci.* 2009, 2, 466.
- [48]. J. Zhu, T. Sun, J. Chen, W. Shi, X. Zhang, X. Lou, S. Mhaisalkar, H.H. Hng, F. Boey, J. Ma, Q. Yan, *Chem. Mater.* 2010, 22, 5333.
- [49]. P.N. Alboni, X. Ji, J. He, N. Gothard, J. Hubbard, T.M. Tritt, *J. Electro. Mater.* 2007, 36, 711.
- [50]. D.L. Medlin, G.J. Snyder, *Curr. Opin. Colloid Inter. Sci.* 2009, 14, 226.
- [51]. J.P. Heremans, C.M. Thrush, D.T. Morelli, *Phys. Rev. B* 2004, 70, 115334.
- [52]. G. Rogl, A. Grytsiv, K. Yubuta, S. Puchegger, E. Bauer, C. Raju, R.C. Mallik, P. Rogl, *Acta Mater.* 2013, 95, 201.
- [53]. G.X. Liang, Z.H. Zheng, P. Fan, J.T. Luo, J.G. Hu, X.H. Zhang, H.L. Ma, B. Fan, Z.K. Luo, D.P. Zhang, *Sol. Energ. Mat. Sol. C.* 2018, 174, 263.
- [54]. L. Yong, L.D. Zhao, Y.C. Liu, J.L. Lan, X. Wei, L. Fu, B.P. Zhang, D. Berardan, N. Dragoë, Y.H. Lin, C.W. Nan, J.F. Li, H.M. Zhu, *J. Am. Chem. Soc.* 2011, 133, 20112.
- [55]. J.L. Lan, Y.C. Liu, B. Zhan, Y.H. Lin, B.P. Zhang, X. Yuan, W.Q. Zhang, W. Xu, C.W. Nan, *Adv. Mater.* 2013, 25, 5086.

## Figure Captions

**Figure 1** (a) Powder X-ray diffraction of CoSb<sub>3</sub> based thin films after annealing, (b) the refined lattice parameter as a function of actual Ti content obtained by energy-dispersive X-ray spectrum. The inset in (b) shows the lattice parameter as a function of the nominal Ti content  $x$  for Ti <sub>$x$</sub> Co<sub>4</sub>Sb<sub>12</sub> in this study and previous reported results.

**Figure 2** Room-temperature Raman scattering spectra of the Ti doped and un-doped thin film specimens.

**Figure 3** SEM images of samples S0, S1 and S3.

**Figure 4** (a) HRTEM image of the S3, (b) The AFM and the SEM images of the precursor Ti layer; (c) The schematic illustration of the thin film growth process: (1) Ti layer with nano thickness, (2) CoSb<sub>3</sub> growing on the Ti layer, (3) After annealing

**Figure 5** (a) the room temperature carrier concentration  $n$  and Hall mobility  $\mu$  for all the samples, (b) the temperature dependence of electrical conductivity  $\sigma$ .

**Figure 6** (a) Seebeck coefficient of the thin films as a function of temperature, (b) room-temperature total thermal conductivity  $k$  and the calculated lattice thermal conductivity  $k_{\text{lat}}$ , (c) the various phonon scattering mechanisms by nano-structure and Ti based points defect, (d) temperature dependence of the ZT value.

**Figure 7** The continuous response of the detector and the peaks corresponding to the values obtained when the finger touched instantly the region of the Cu contact.

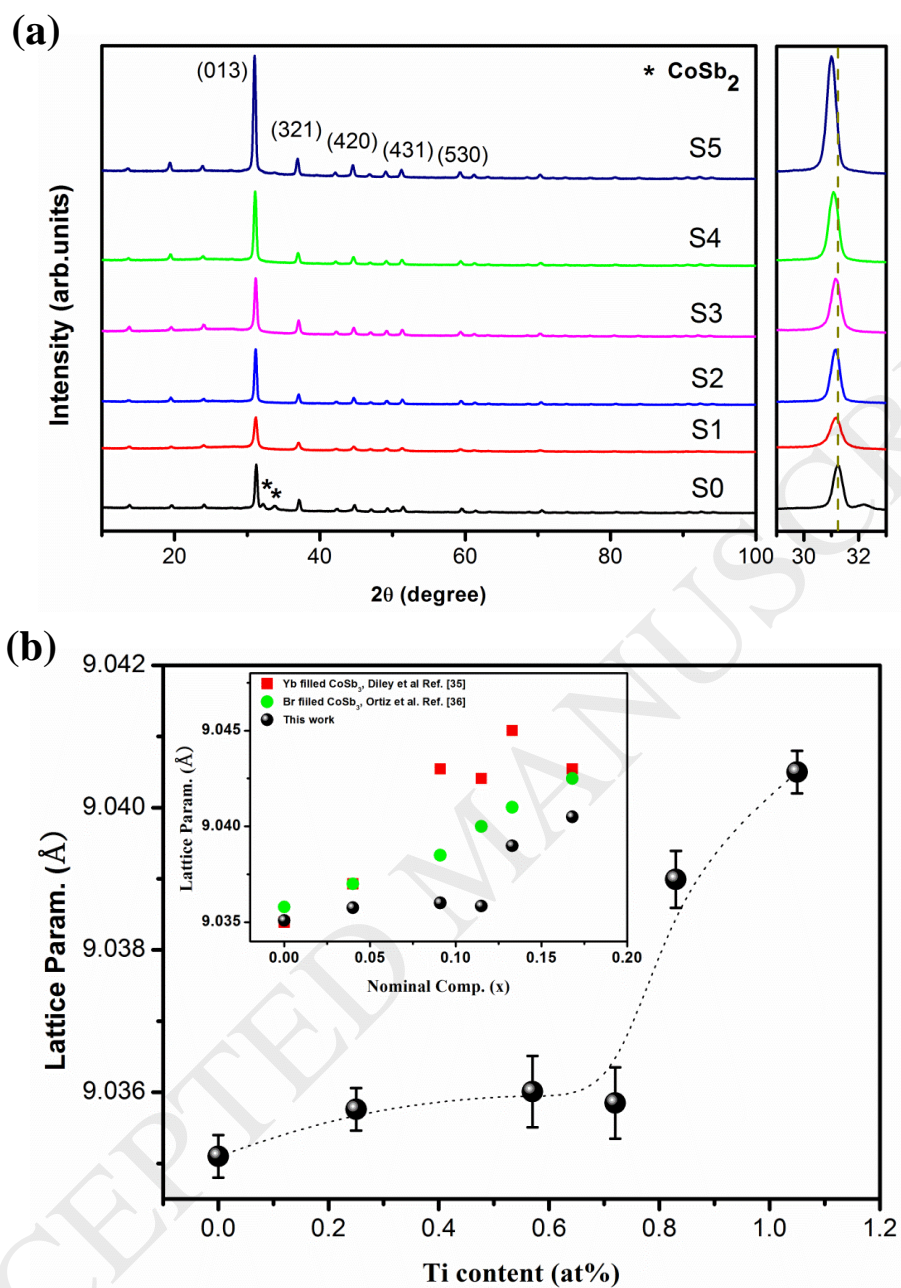


Figure 1

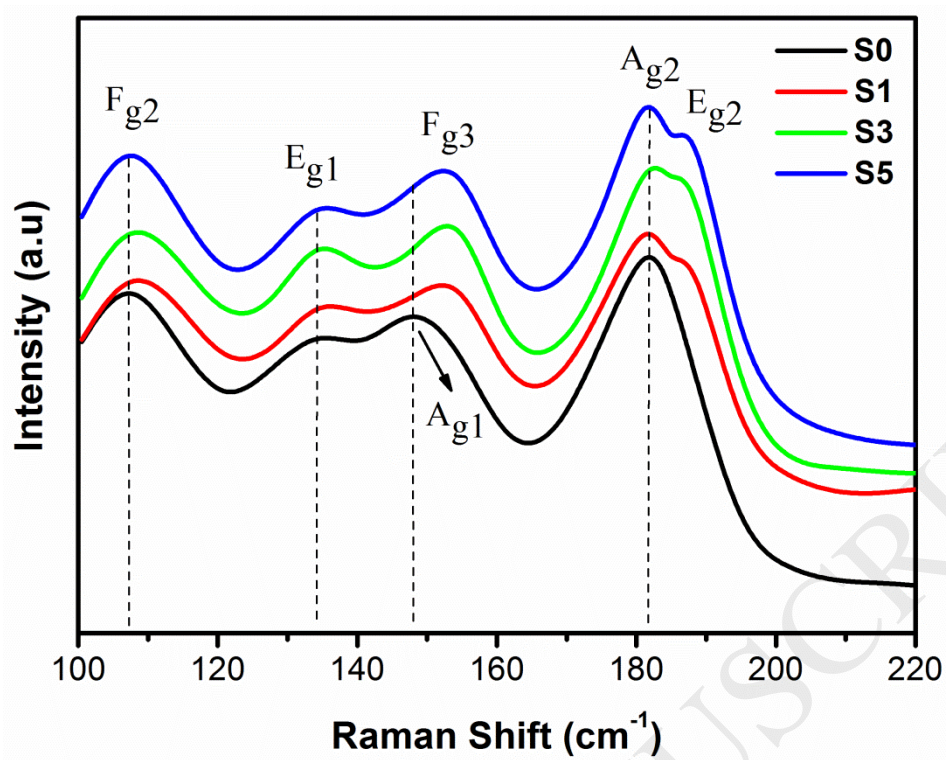


Figure 2

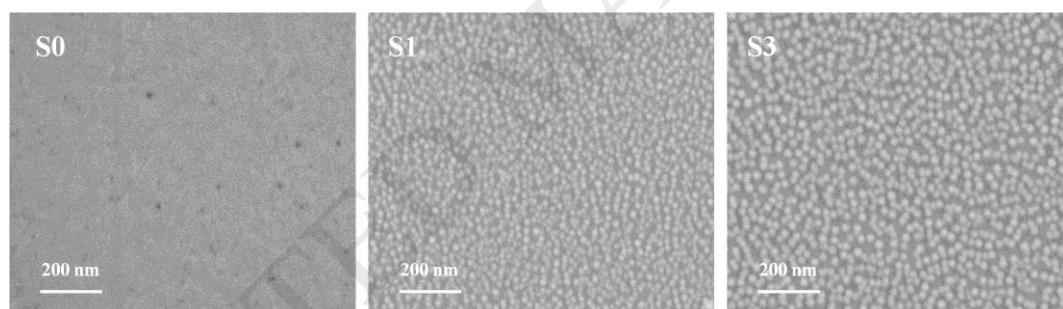


Figure 3

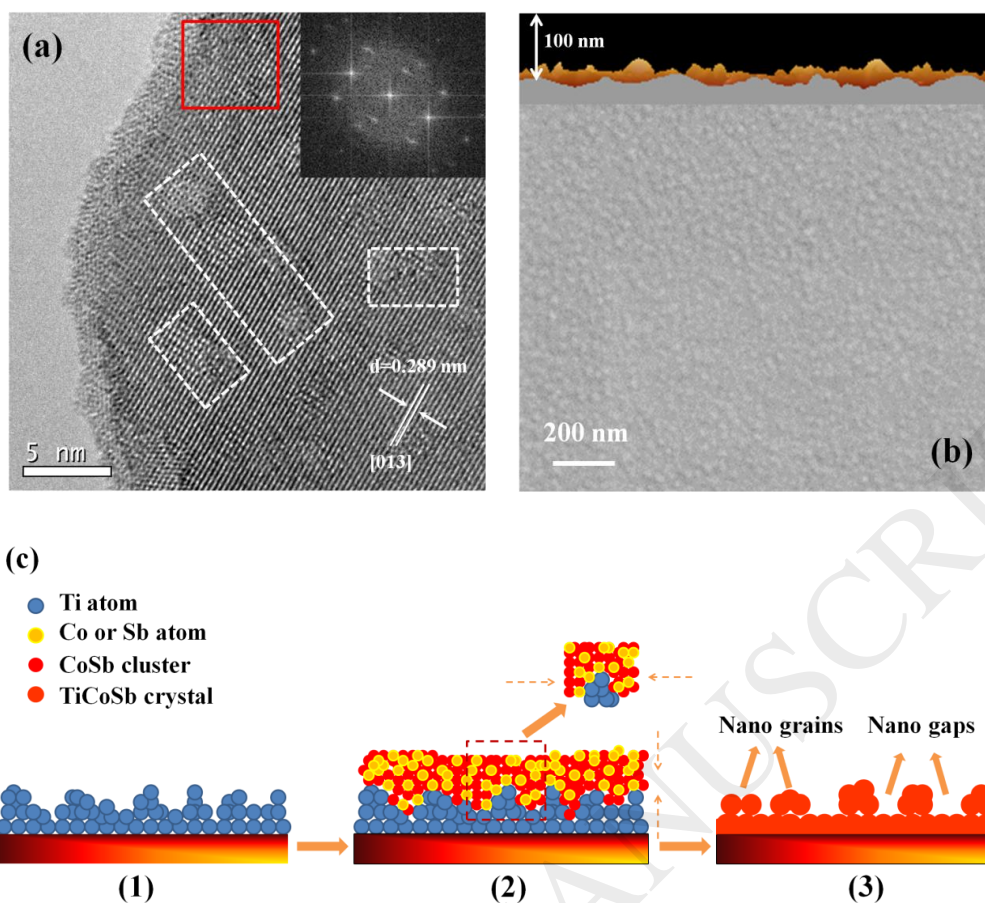


Figure 4

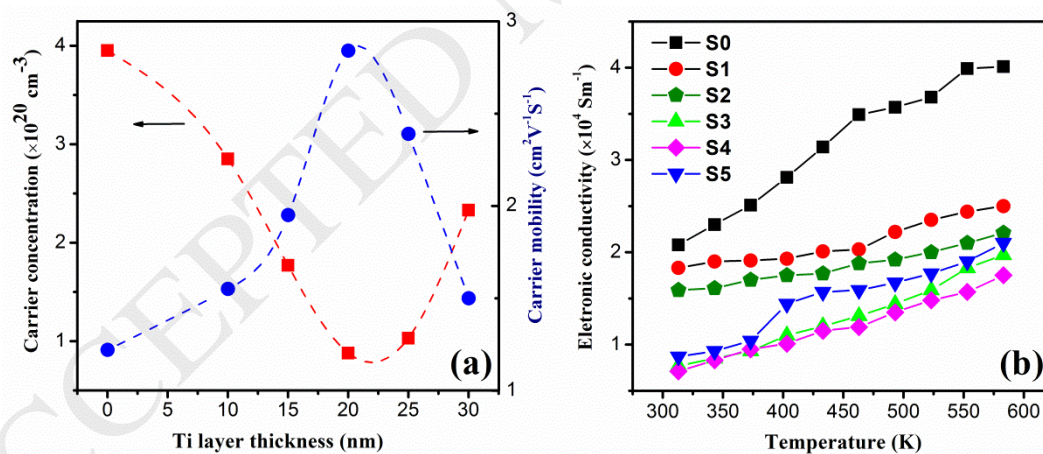


Figure 5

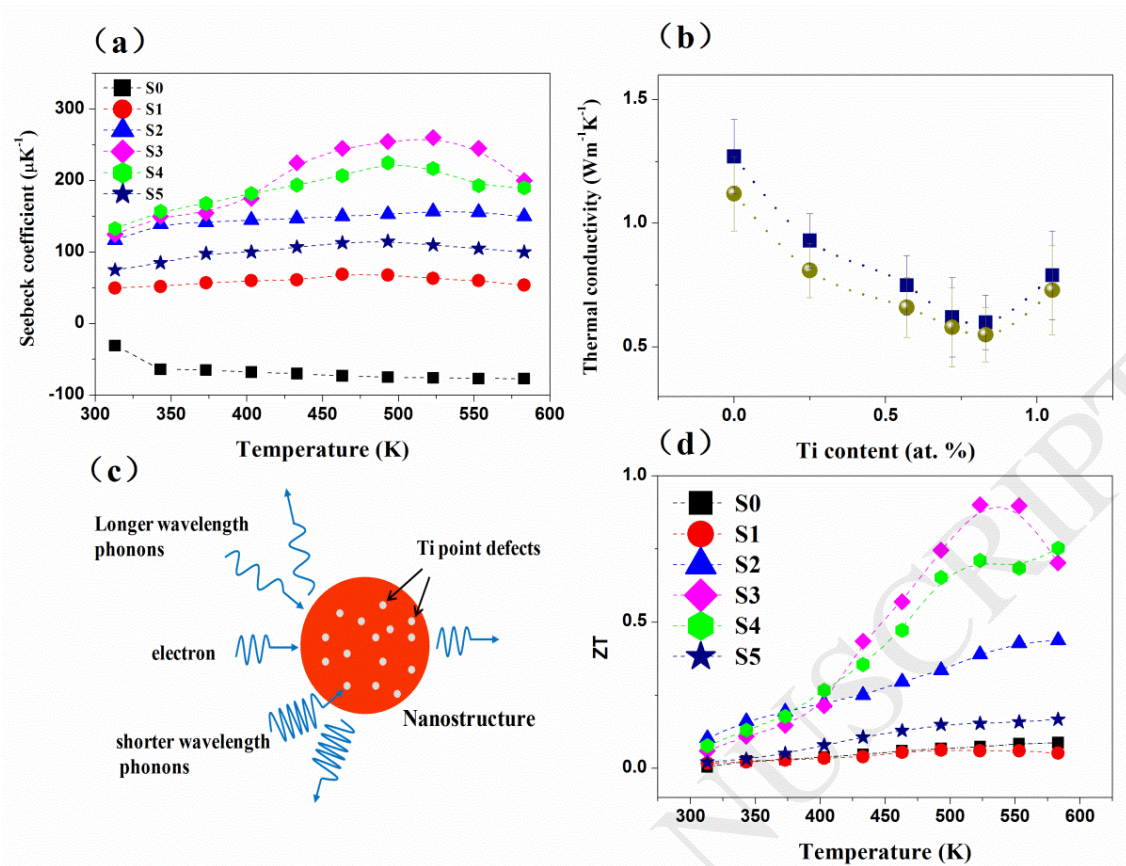


Figure 6

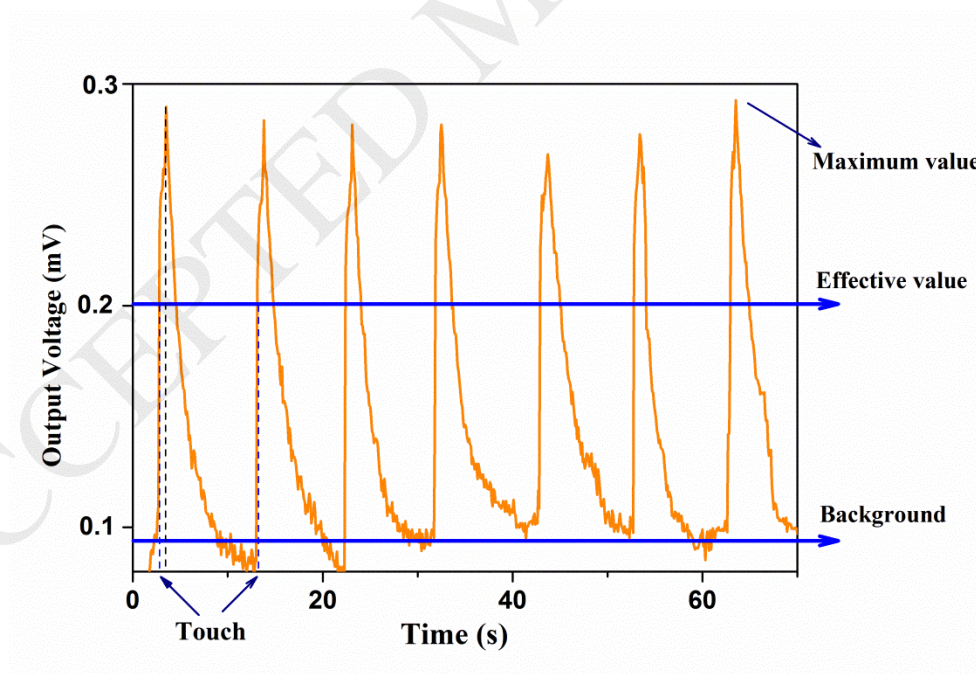


Figure 7

**Table**

Table 1 Actual Ti contents for the thin films

	S0	S1	S2	S3	S4	S5
Thickness of Ti (nm)	0	10	15	20	25	30
Ti (at. %)	0	0.25	0.57	0.72	0.83	1.05

Table 2 The calculated formation energy

System	Ti <sub>Co</sub>	Ti <sub>Sb</sub>	Ti <sub>i</sub>	Ti <sub>i+Sb</sub>	Ti <sub>2i+Sb</sub>
Formation energy (eV)	1.68	0.18	2.52	0.88	0.08